Multi-Physics-based FEM Analysis for Post-voiding Analysis of Electromigration Failure Effects*

(Invited Paper)

Hengyang Zhao[1] and Sheldon Tan[1]

[1]Department of Electrical and Computer Engineering, University of California, Riverside, CA

ABSTRACT

In this paper, we propose a new multi-physics finite element method (FEM) based analysis method for void growth simulation of confined copper interconnects. This new method for the first time considers three important physics simultaneously in the EM failure process and their time-varying interactions: the hydrostatic stress in the confined interconnect wire, the current density and Joule heating induced temperature. As a result, we end up with solving a set of coupled partial differential equations which consist of the stress diffusion equation (Korhonen's equation), the phase field equation (for modeling void boundary move), the Laplace equation for current density and the heat diffusion equation for Joule heating and wire temperature. In the new method, we show that each of the physics will have different physical domains and differential boundary conditions, and how such coupled multi-physics transient analysis was carried out based on FEM and different time scales are properly handled. Experiment results show that by considering all three coupled physics – the stress, current density, and temperature – and their transient behaviors, the proposed FEM EM solver can predict the unique transient wire resistance change pattern for copper interconnect wires, which were well observed by the published experiment data. We also show that the simulated void growth speed is less conservative than recently proposed compact EM model.

CCS CONCEPTS

• **Hardware → Temperature simulation and estimation**; *Power grid design*; **Hardware reliability**;

KEYWORDS

Electromigration, IC Relibility, Finite Element Method

ACM Reference Format:

Hengyang Zhao[1] and Sheldon Tan[1]. 2018. Multi-Physics-based FEM Analysis for Post-voiding Analysis of Electromigration Failure Effects: *(Invited Paper). In IEEE/ACM INTERNATIONAL CONFERENCE ON COMPUTER-AIDED DESIGN (ICCAD'18), November 5–8, 2018, San Diego, CA, USA. ACM, New York, NY, USA, 8 pages. https://doi.org/10.1145/3240765.3243486*

* This work is supported in part by NSF grant under No. CCF-1527324, and in part by NSF grant under No. CCF-1741961, in part by DARPA grant under No. HR0011-16-2-0009.

ICCAD, 2018, San Diego, CA, USA

ACM ISBN 978-1-4503-5950-4/18/11…$15.00
https://doi.org/10.1145/3240765.3243486

1 INTRODUCTION

Electromigration (EM) is the top reliability killer for copper based interconnects of current integrated circuits (ICs) in 10 nm technology and below. 2014 ITRS predicts that the required current density for driving a normal gate will exceed the EM current density limit in 2024 [14, 17] if the industry continues current technology scaling with existing interconnect materials and EM design rules based on current density.

To mitigate this coming EM crisis, one important strategy is to leverage the more accurate and less conservative EM models, as the existing EM models — the Black's equation [5] and Bleck's immortality check [6] — are too conservative and can leads to excessive overdesign and subject to growing criticism [13]. As a result, more accurate physics-based EM modeling and assessment techniques are critical for EM-aware physical design and system level EM lifetime optimization [24].

Recently, a number of new physics-based EM modeling approaches have been proposed [7, 8, 10, 13, 21–23]. Those methods start with Korhonen's partial diffusion equation which describes dynamics between the EM-induced stress and stress-induced back force or atom migrations [16]. Existing approaches either seek for closed form solutions for single segment or simple wire structures under blocked material boundary conditions [7, 8, 13, 22], or solve Korhonen's equation using numerical methods such as finite difference and eigen function method [10, 26]. However, all of those methods mainly focus on the void nucleation phase in which the tensile stress at the cathode gradually reaches the critical stress, then voids start to form. The void growth phase, which is very important for determining the final failure of EM (resistance change of the interconnect), however, were modeled by some simple, less accurate models in those methods. The void growth phase was much less studied as the modeling and analysis task for the process of void growth is a notoriously difficult task. The reason are as follows: First, void growth phase is a multi-physics process in which stress evolution, current density distribution, and thermal impact due to Joule heating are all important for determining the resistance change over time. Second, void shapes or their volumes and boundaries keep changing, which will cause numerical problems using finite element method as very small meshes thus large system matrices will be generated. We remark that when the compressive stress at the anode continues to be built up, hillocks or extrusion will form, which can potentially cause short-circuit failures. But the void nucleation is still the dominant EM failure process as the critical threshold for tensile stress is lower than that of compressive stress in general [12, 17].

Recently, work [21] proposed a one-dimensional solution for the void growth analysis based on Korhonen's equation. But this method fails to consider the void volume change and its impact on the stress distribution, which was shown important for void growth speed. Bhate *et al* [4] proposed a 2D finite element method (FEM) based void growth analysis method by considering stress and void growth using coupled diffusion equations. The Cahn-Hilliard equations are coupled to model the voids with shapes changing over time. But the interaction between void volume and stress distributions was also not considered as well. To mitigate this problem, Zhao *et al* proposed a 3D finite element method (FEM) based post-voiding analysis method [28]. In this method, the interplay between void growth and evolving stress distribution in the remaining interconnect is explicitly modeled to consider physics-based conservation constraint taken into account by introducing a separate phase field to model the void boundary evolution process. The resulting two coupled partial differential equations (in addition to the dynamic stress field partial differential equation) are solved to analysis the void volume growth over time. However, this method still does not consider the interaction between different physics as mentioned earlier.

In this paper, we propose a novel multi-physics finite element method (FEM) based solution for void growth simulation of confined copper interconnects for EM failure analysis. Our contributions lies in the following aspects: First, for the first time, three important physics and their transient interactions are considered simultaneously in the new method: the hydrostatic stress in the confined interconnect wire, the current density and Joule heating induced temperature. Second, we end up solving a coupling partial differential equations which consists of stress differential equation (Korhonen's equation), the phase field equation (for modeling void boundary move), the Laplace equation for current density and the heat diffusion equation for Joule heating and wire temperature. We show that each of the physics will have different physical domains and corresponding boundary conditions, and how such coupled multi-physic FEM transient analysis was carried out, and how different time scales are properly handled. Last but not least, numerical results show that by considering all three coupled physics — the stress, current density, and temperature — and their transient behaviors, the proposed FEM post-void EM solver can predict the unique transient wire resistance change pattern in which resistance jump happens when void grows to the critical volume for copper interconnect, which were well observed by published experiment data. We also show that the simulated void growth speed is less conservative than a recently proposed compact EM model.

This paper is a part of the ICCAD 2018 special session on *A Journey from Physics to System Level on the Reliability Tracks*. The other three papers of this special session are [18], [19] and [2].

2 PROBLEM FORMULATION

In this section, we present the multi-physics simulation problem that we are facing to model and characterize the post-voiding process in a confined copper interconnect. Fig. 1 shows an *up-stream* interconnect wire structure in which the electron flux is flowing from the bottom metal wire (metal 1 or M1) through the via and into the upper metal (metal 2 or M2).

As we can see, basically we have three physics involved and three overlapped simulation domains accordingly. First is the hydrostatic stress evolution in the copper metal, which is marked as the brown in the figure. Stress will be developed once the current is applied in M2 (for up-stream, we only focus on M2 as void will be developed

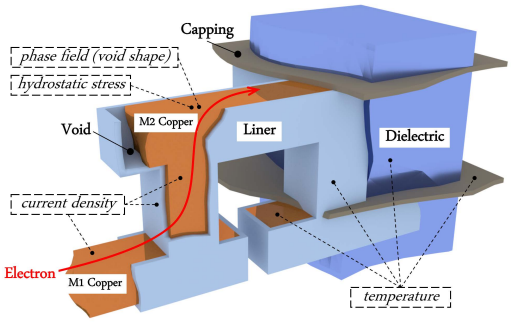

Figure 1: 3D illustration of up-stream interconnect structure and simulated physical systems.

in the cathode, which is to the left of M2). This is called copper wire domain Ω_C and stress on the metal 2 will be governed by the stress differential equation shown below. The second domain is related to the electrical current density , which consists of both copper and barrier or liner surrounding the copper as current can flow through both the copper and the liner. We refer it as the wire domain or Ω_W and it will be described by the Laplace equation of electrical potential. The third domain is the thermal related domain, which consists of everything: copper, liner, capping layers, surrounding dielectric material. We call this thermal domain or Ω_T.

As we can see, all three physics are coupled in this EM post-voiding analysis process: current density and temperature will have impacts on the stress development; void growth will change the current density distribution over time, which will change both current density and temperature profile; and eventually the resistance of the interconnect will change, which is the key determination of the EM failure criteria.

2.1 Hydrostatic stress modeling in post-voiding phase

For the stress evolution in a confined metal (by blocking materials, terminals, or vias), the stress can be modeled by the Korhonen's hydrostatic stress diffusion equation [16]:

$$\frac{\partial \sigma}{\partial t} = \nabla \cdot \left(\frac{D_a B}{k_B T} (\Omega \nabla \sigma - eZ\rho \vec{j}) \right) \quad \text{in } \Omega_C, \tag{1}$$

$$\nabla \sigma = \frac{eZ\rho \vec{j}_N}{\Omega} \quad \text{on } \partial\Omega_C \cap \Gamma_N, i = 1, ..., k, \tag{2}$$

$$\nabla \sigma = \frac{\sigma}{\delta} \quad \text{on } \partial\Omega_C \cap \Gamma_{\text{void}}, \tag{3}$$

where σ is hydrostatic stress, product eZ is effective charge of the migrating atoms, ρ is electrical resistivity, $\vec{j}$ is current density, k_B is the Boltzmann constant, δ is the effective thickness of the copper-void boundary, T is the operating temperature, and E_a is the EM activation energy. Ω_C is the domain of simulated copper interconnect and $\partial\Omega_C$ denotes its boundary. Γ_N is the flux termination boundaries, where normal current density $\vec{j}_N$ are prescribed. Γ_{void} denotes the void boundary, which can be a union of several discrete voids. D_a is the atomic diffusion coefficient. D_a is given by $D_a = D_0 \exp(-E_a/(k_B T))$ where D_0 is the diffusion coefficient. Copper grain size is a key factor that affects EM lifetime [20]. Effective diffusion coefficient can be much higher in copper grain boundaries than grain bodies, which leads to different D_0 over the

copper interconnect. In equation (1), a uniform D_0, synthesized from different body and boundary diffusion coefficients, is used. Note that Korhonen's hydrostatic diffusion equations can be applied to 3D multi-segment interconnect with multiple flux-termination boundary nodes, allowing any number of evolving voids to be simulated.

For post-voiding analysis, there is an important constraint needs to be considered. The void volume and the stress integral of the remaining wire are correlated by the following atom conservation equation [15]

$$V_S = \frac{1}{B}\int_{\Omega_C} \sigma dV, \tag{4}$$

where Ω_C is the volume of remaining interconnect, V_S is void volume, and B is the effective bulk modulus. However, most of the existing post-void simulation methods fail to consider this void volume conservation constraint. To mitigate this problem, In [28], a phase field variable ϕ was introduced model the interaction of stress σ and void shape (implied by phase field variable), which is governed by the following equation:

$$\frac{\partial \phi}{\partial t} = \frac{1}{\tau_\phi}\left(\frac{\delta^2}{2}\nabla^2\phi + \phi(1-\phi^2)\right) - k_R\vec{v}\cdot\nabla\phi, \tag{5}$$

where δ is the thickness of the void-copper diffusive boundary, τ_ϕ is the stabilizing time constant, $\vec{v}$ is the velocity of phase field boundary and k_R is regulation factor, which is defined below:

$$k_R = \frac{1}{2}\left(1 + \mathrm{erf}(V_W - V_S)\right), \tag{6}$$

where $\mathrm{erf}(\cdot)$ is the Gauss error function to force a bounded output range $(-1, 1)$ and V_W is defined below:

$$V_W = \int_{\Omega_C}\left(w_V + \frac{1}{2}w_B\right)dV, \tag{7}$$

where w_V and w_B are the weighted functions for void and boundary sections of a void. Introduction of k_R, which is a function of the difference between the actual volume V_W and volume acquired from the conservation (4), V_S, will ensure that the conservation is met [28].

2.2 Current density modeling

The second physics to be modeled is the current density distribution in a wire as the current density $\vec{j}$ is an important variable in the Korhonen's equation 1 and varies significantly around intersections and corners, where voids are often form or evolve at.

The steady-state (electrostatic) electric field in an interconnect, can be modeled by the Laplace equation with Dirichlet and Neumann boundary conditions. Specifically, for electrical field in the steady state, we have

$$\vec{E} = -\nabla V,\ \vec{j} = \frac{1}{\rho}\vec{E}, \tag{8}$$

where V is the voltage potential, $\vec{E}$ is the electric field, and $\vec{j}$ is the current density, and ρ is the electrical resistivity. Given the conservation of charge carriers, current density $\vec{j}$ must have zero divergence over the conductor:

$$0 = \nabla\cdot\vec{j} = -\nabla\cdot\left(\frac{1}{\rho}\nabla V\right). \tag{9}$$

In general, the steady state electrical potential V can be prescribed by the Laplace equation with both Dirichlet (voltage) and Neumann (current density) boundary conditions given as follows:

$$\nabla\cdot\left(\frac{1}{\rho}V\right) = 0,\ \text{in } \Omega_W, \tag{10}$$

$$V = u_V,\ \text{on } \partial\Omega_W \cap \Gamma_V, \tag{11}$$

$$\nabla V\cdot\vec{n} = g_V,\ \text{on } \partial\Omega_W \cap \Gamma_I, \tag{12}$$

where Ω_W is the domain of conductor including copper and liner, Γ_V is the boundaries where voltage (Dirichlet) boundary conditions are given, Γ_I is boundaries where current density (Neumann) boundary conditions are given, V is the unknown electrical potential to be found, u_V, and g_V are given voltage sources and current sources at the boundaries.

2.3 Thermal modeling in a confined wire

In the circuit and layout level, the heat transfer phenomena are governed by the following heat differential equation [3, 9]:

$$\rho_M C_p\frac{\partial T}{\partial t} - \nabla\cdot(\kappa\nabla T) = g_T, \tag{13}$$

subject to the following convectional thermal boundary condition (Robin boundary condition)

$$\kappa\nabla T\cdot\vec{n} = h(T_{\text{ext}} - T). \tag{14}$$

Here, T is the temperature (K), ρ_M is the mass density of the material ($\mathrm{kg}\cdot\mathrm{m}^{-3}$), C_p is the mass heat capacity ($\mathrm{J}\cdot\mathrm{kg}^{-1}\cdot\mathrm{K}^{-1}$), κ is the thermal conductivity ($\mathrm{W}\cdot\mathrm{m}^{-1}\cdot\mathrm{K}^{-1}$), and g_T is the heat energy generation rate ($\mathrm{W}\cdot\mathrm{m}^{-3}$), $\vec{n}$ is the outward direction normal to the boundary, h is the heat-transfer coefficient ($\mathrm{W}\cdot\mathrm{m}^{-2}\cdot\mathrm{K}^{-1}$), and T_{ext} is the ambient temperature surrounding the thermal system. If $h = 0$, the boundary condition is adiabatic (convectionally isolated), otherwise it is convective. Note that the thermal conductivity κ differs for different materials.

For a copper wire with surrounding liners, capping layers, and dielectrics, which all together are defined as the domain Ω_T, the heat source comes from Joule heating effect. As a result, we have

$$g_T = j^2\rho \tag{15}$$

In our work, we assume that κ is constant for each material. Then, (13) can be written as

$$\rho_M C_p\frac{\partial T}{\partial t} - \kappa\nabla^2 T = j^2\rho_M,\quad \text{in } \Omega_T, \tag{16}$$

$$\kappa\nabla T\cdot\vec{n} = h(T_{\text{ext}} - T),\quad \text{on } \partial\Omega_T \cap \Gamma_T, \tag{17}$$

subject to the initial condition $T = T_0$ at $t = 0$, where Γ_T is the boundary surface for Robin boundary conditions.

2.4 The multi-physics coupled simulation problem

Now have discussed each important aspects of the EM post-voiding physics. It is time to put all the related partial differential equations (PDE) together for the proposed multi-physics EM post-voiding simulation problem. The following equations govern the hydrostatic stress and void shape evolution in an interconnect Ω_C, (consisting of void, void-copper boundary, and copper) in a confined metal wire, the electrical potential (for current density analysis) in the

wire domain Ω_W, and the temperature in the thermal domain Ω_T:

$$\frac{\partial \sigma}{\partial t} = w_C \nabla \cdot \left(\frac{D_a B}{k_B T} (\Omega \nabla \sigma + eZ\rho j) \right) + w_V \frac{\sigma}{\tau_{\text{void}}} + w_B \left(\nabla \cdot \left(\frac{D_a B \Omega}{k_B T} \nabla \sigma \right) - \frac{\sigma v k_\tau}{\delta} \right), \text{ in } \Omega_C, \tag{18}$$

$$\frac{\partial \phi}{\partial t} = \frac{1}{\tau_\phi} \left(\frac{\delta^2}{2} \nabla^2 \phi + \phi(1-\phi^2) \right) - k_R \frac{D_a \Omega}{k_B T} \nabla \sigma \cdot \nabla \phi, \text{ in } \Omega_C, \tag{19}$$

$$\nabla \cdot \left(\frac{1}{\rho} \nabla V \right) = 0, \text{ in } \Omega_W \tag{20}$$

$$\rho_M C_p \frac{\partial T}{\partial t} = \nabla \cdot (\kappa \nabla T) + j^2 \rho, \text{ in } \Omega_T, \tag{21}$$

subject to corresponding boundary conditions (2), (11), (12), and (14).

3 FINITE ELEMENT METHOD IMPLEMENTATION

In this section, variational formulations that is implemented in the simulation software are listed, followed by the description of adaptive local mesh refinement, and a brief review of the software architecture.

3.1 Variational formulation

Based on FEniCS FEM library[1], a program is built to implement the above-mentioned dynamic system. Variational weak form is the bridge that connects the mathematical strong form of variables such as ϕ and σ and the software implementation of solving them. Therefore we list the weak forms of the simulated systems in the rest of this section. In the weak form equations, we use $x^{(n)}$ to denote the value of x at the nth simulated time step.

We list the derived weak form equations of electrical potential V, phase field ϕ, temperature T, and hydrostatic stress σ in the following.

Electrical potential: Since EM analysis is done on a time scale of at least days, we treat the electrical potential distribution V as quasi static so it can be described by the strong form Laplace equation (10). Multiply shape function φ on both side of equations (10) and (11), the corresponding electrical potential weak form can be derived by applying divergence theorem:

$$\int_{\Omega_C} \nabla V \cdot \nabla \varphi \, dV = \int_{\partial \Omega_C} g_V \varphi \, dS, \tag{22}$$

where dV is for volume integration and dS is for the surface integration.

Phase field: To discretize time variable t in equation (19), we respectively substitute $\partial\phi/\partial t$ with $\frac{1}{\Delta t}\left(\phi^{(n)} - \phi^{(n-1)}\right)$, ϕ with $\theta\phi^{(n)} + (1-\theta)\phi^{(n-1)}$ to numerically solve the equation based on Euler method. The superscript n is for time step index. By applying divergence theorem and collect $\phi^{(n)}$ related terms on the left hand side, we have the time-discretized weak form of equation (19)

$$\begin{aligned} &\int_{\Omega_C} \phi^{(n)} \varphi \, dV + \int_{\Omega_C} \frac{\delta^2 \theta \Delta t}{2\tau_\phi} \nabla \phi^{(n)} \cdot \nabla \varphi \, dV \\ &= \int_{\Omega_C} \phi^{(n-1)} \varphi \, dV - \int_{\Omega_C} \frac{\delta^2 (1-\theta) \Delta t}{2\tau_\phi} \nabla \phi^{(n-1)} \cdot \nabla \varphi \, dV \\ &+ \int_{\Omega_C} \frac{\Delta t}{\tau_\phi} (\phi^{(n-1)} - (\phi^{(n-1)})^3) \varphi \, dV \\ &- \int_{\Omega_C} \Delta t k_R \vec{v} \cdot \nabla \phi^{(n-1)} \varphi \, dV. \end{aligned} \tag{23}$$

Here θ is the Euler method controller ($\theta = 0$: backward Euler; $\theta = 1$: forward Euler; $\theta = \frac{1}{2}$: mixed Euler or Crank-Nicolson method). We use Crank-Nicolson method ($\theta = \frac{1}{2}$) since it has the stability like backward Euler method and also higher (second order) accuracy. Δt is the time discretization step which is a knob for controlling solution accuracy.

Temperature: By applying similar technique while substituting $\partial T/\partial t$ with $\frac{1}{\Delta t}\left(T^{(n)} - T^{(n-1)}\right)$, T with $\theta T^{(n)} + (1-\theta)T^{(n-1)}$, the time-discretized weak form is derived:

$$\begin{aligned} &\int_{\Omega_T} \rho_M c_p T^{(n)} \varphi dV + \int_{\Omega_T} k_T \Delta t \theta \nabla T^{(n)} \cdot \nabla \varphi dV \\ &+ \int_{\partial \Omega_T} \Delta t \theta h T^{(n)} \phi dS \\ &= \int_{\Omega_T} \rho_M c_p T^{(n-1)} \varphi dV - \int_{\Omega_T} k_T \Delta t (1-\theta) \nabla T^{(n-1)} \cdot \nabla \varphi dV \\ &- \int_{\partial \Omega_T} \Delta t (1-\theta) h T^{(n-1)} \phi dS + \int_{\partial \Omega_T} \Delta t h T_{\text{ext}} \phi dS \\ &+ \int_{\Omega_T} \left(j^{(n-1)} \right)^2 \rho \left(\phi^{(n-1)}, T^{(n-1)} \right) \Delta t \varphi dV. \end{aligned} \tag{24}$$

Hydrostatic stress: We perform similar time discretization and mathematics techniques on hydrostatic variable σ to get the following weak form of equation (2) and (18)

$$\begin{aligned} &\int_{\Omega_C} \left(1 + \left(\frac{w_V}{\tau_{\text{void}}} - \frac{|v| k_\tau w_B}{\delta} \right) \theta \Delta t \right) \sigma^{(n)} \varphi \, dV \\ &+ \int_{\Omega_C} (w_B + w_C) \frac{D_a B \Omega}{k_B T} \theta \Delta t \nabla \sigma^{(n)} \cdot \nabla \varphi \, dV \\ &= \int_{\Omega_C} \left(1 - \left(\frac{w_V}{\tau_{\text{void}}} - \frac{|v| k_\tau w_B}{\delta} \right) (1-\theta) \Delta t \right) \sigma^{(n-1)} \varphi \, dV \\ &- \int_{\Omega_C} (w_B + w_C) \frac{D_a B \Omega}{k_B T} (1-\theta) \Delta t \nabla \sigma^{(n-1)} \cdot \nabla \varphi \, dV \\ &+ \int_{\Omega_C} \Delta t w_C \frac{D_a B \Omega}{k_B T} eZ \nabla \sigma^{(n-1)} \cdot \nabla \varphi \, dV \\ &+ \int_{\partial \Omega_C} \Delta t w_C \frac{D_a B}{k_B T} eZ \rho j_{N_i} \cdot \vec{n} \varphi \, dS, \end{aligned} \tag{25}$$

where j_N denotes the prescribed normal current densities as described in (2).

With the weak forms (22) (23) and (25), the EM solver is able to calculate integrals to assemble FEM matrices and input loads and solve for the space- and time-discretized solutions.

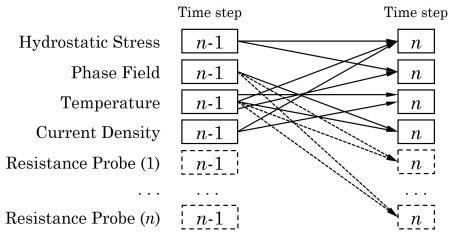

Figure 2: Block diagram of time dependent FEM systems coupling.

3.2 Software implementation

All four coupled physics variables — hydrostatic stress σ, material phase field ϕ, temperature T, and voltage V — are designed to be depend on each others only by means of data transferring. But they are highly decoupled in terms of logic organization, allowing any number of resistance probes, acting as same-level physics variables as the four, to be easily configured and plugged in. The data dependency between each time step is depicted in Fig. 2, where at time step n, all the systems (related physics equation) depend on the previous time step $n-1$ to solve. Take temperature as an example, it serves as a necessary prerequisite of itself because of the thermal diffusion nature over time. Temperature also has impacts on voltage (current density analysis and all resistance probes) by affecting material electrical conductivity. It also has impacts on hydrostatic stress by affecting material activation energy and diffusion coefficient, and on phase field by affecting material diffusion coefficient in a similar way.

As mentioned above, user is able to setup any number of resistance probes by composing corresponding configuration inputs. The simulator will set aside a separate physical system, only focusing on the wire domain Ω_W, and calculating the resistance between the specified anode and cathode. For each configured resistance probe, the simulator will ground the cathode and apply a fixed inward normal current density on the anode, and then calculate the effective resistance by applying Ohm's law. As the arrows implies in Fig. 2, all resistance calculations will be separately done. Thereby their Joule heating effect will not be coupled with the temperature variable, nor their electromigration effect with the hydrostatic stress variable.

The proposed method is implemented using FEniCS FEM library [1], programmed in Python 3. The work flow can be divided into the following parts:

(1) The user prepares for the input structure in XML format supported by FEniCS. FEniCS supports conversion from a variety of widely-used geometry description format to the XML format that it supports. Currently in the experiments, Gmsh [11] format version 2.2 is used to describe the input structure and create mesh. Thanks to the `Include` directive that Gmsh supports, the input geometry is allowed to be separated into two parts, dimension definition and actual code describing the geometry and physical entities. This allows the geometry to be programmatically controlled for a parameter sweep if needed.
(2) The user prepares for the configuration for the simulator. The configuration file contains all the adjustable parameters, include boundary conditions of the system PDEs, resistance probe deployments, a large number of material parameters such as bulk modulus B and resistance ρ, and finite element method parameters such as time step control, solver selection, error control, etc. The user configuration is also designed to allow nesting and overwriting, which is for the sake of the automation of parameter sweep as well.
(3) The user runs the simulator program. The simulator can be configured to periodically generate output as well as snapshots. The output is in VTK format [25], which is widely used in scientific computing community for scalable and efficient post-processing and rendering. The snapshots are designed to allow user save-and-load the simulation if to rerun the simulator with different parameters, such as finer time discritization.
(4) The user performs analysis on the results. Geometry dependent results (scalar/vector data attached to mesh nodes) are stored as VTK format for further analysis or post-process.

4 EXPERIMENTAL RESULTS AND DISCUSSIONS

In this section, we use three examples to demonstrate the effectiveness of the proposed multi-physics electromigration post-voiding simulation method, and also show the simulated results are consistent with some measured results from experiments on real silicon.

4.1 Two-segment simulation with saturated void

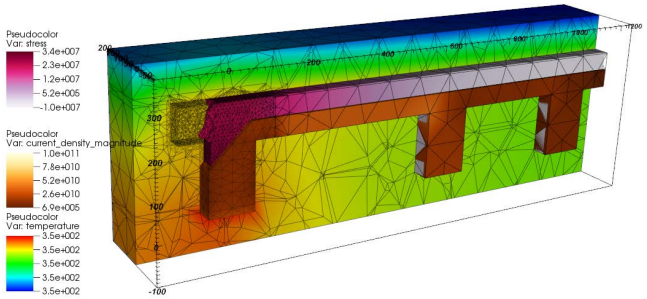

Figure 3: Perspective view of the two-segment simulation result with saturated void.

The first example is a two-segment interconnect wire as shown in Fig. 3. The leftmost via is connected to ground and the rest of the two vias are respectively prescribed inward normal current density of $2\times10^{10}\mathrm{A}\cdot\mathrm{m}^{-2}$ and $1\times10^{10}\mathrm{A}\cdot\mathrm{m}^{-2}$. An initial small void is placed at the reservoir on the cathode (left) node. The wire lengths are respectively 500nm and 300nm, in which case the void will saturate at the cathode end (near the via connected to ground) and not cause failure of resistance increase. Fig. 3 shows the perspective view of all the four simulated physics variables (stress, current density and temperature). The phase field is illustrated by removing the elements where $\phi < 0$ on the stress (σ) plot.

Fig. 4 shows simulated temperature distribution for the two-segment. As we can see, the highest temperature is around bottom of the via as current flows through the barrier, which has higher resistance than the copper, into bottom wire.

Fig. 5 shows the current density results. As we can see, the highest current density happens around the corner of via and main wire branch, which is typocal local field enhancement field. Fig. 6

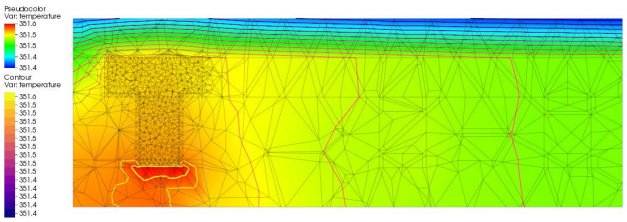

Figure 4: Temperature vertical slice of the two-segment simulation.

shows the simulated stress distribution. As we can see, near-void area has the highest stress, and the stress around and inside void are zero. In this example, the void is saturated at a relatively small volume, which does not have a strong impact the current density distribution. Therefore the wire resistance remained roughly same as void-less situation.

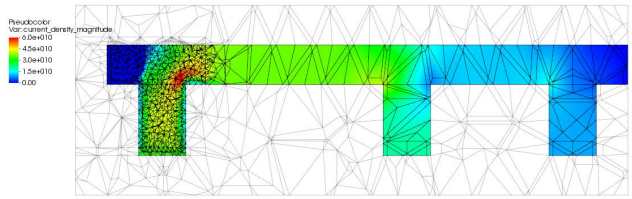

Figure 5: Current density vertical slice of the two-segment simulation.

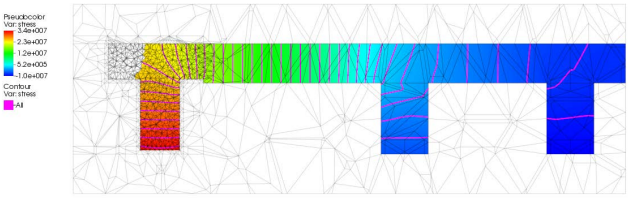

Figure 6: Hydrostatic vertical slice of the two-segment simulation.

4.2 Three-segment simulation with saturated void

The second example is a T-shape three-segment interconnect as shown in Fig. 7. For the sake of the completeness of containing the plots of physics variables in their figures, the wire lengths are chosen to be relatively short as well. The three branches have lengths 500nm, 400nm, and 300nm. Inward normal current densities at vias are prescribed as 2×10^{10}A·m^{-2}, 1×10^{10}A·m^{-2}, and 1×10^{10}A·m^{-2}. Similar to the two-segment experiment, this configuration will also result an immortal wire. Figure 7 shows the perspective view of the simulation results. Figures 8, 9, and 10 provide horizontal sliced results for more details.

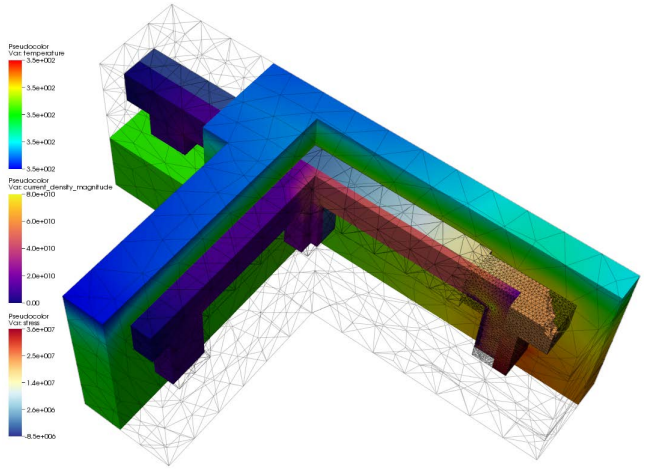

Figure 7: Perspective view of the three-segment simulation result with saturated void.

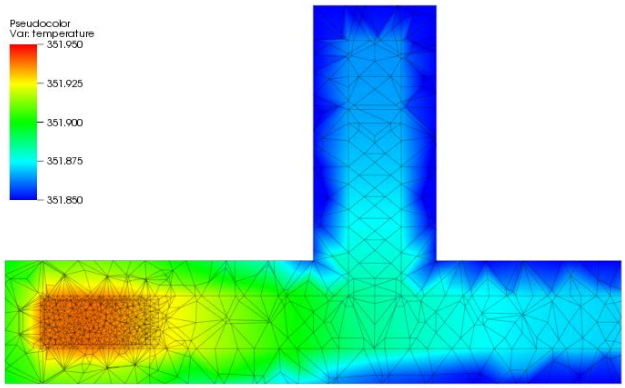

Figure 8: Temperature vertical slice of the three-segment simulation.

4.3 Simulation with wire resistance change

In this example, we investigate the wire resistance change pattern over time when the void is formed and the void grows over the critical volume. We will compare the resistance change against patterns observed in real silicon experiments.

It was observed that the in the failure process of a electromigration, vulnerable interconnect that is upstream-configured, its resistance growth follows a certain pattern [27]. Fig. 11 shows such resistance change patterns, in which the resistance starts with a very slow increasing speed, followed by a sharp jump, and then increases approximately in a linear manner regarding time. The reason of the sharp resistance jump is due to the Joule heating induced resistance jump. This happens when the void completely cuts the copper wire into two separate parts and all the current has to suddenly be shunted to the liner, which has a much higher resistance as shown in Fig. 13.

In the simulation, in order to have an interconnect that will end up with high resistance, we use a straight-connected two-segment structure similar as in the one used in section 4.1, but with wire lengths 20μm and 10μm and same current densities of 2×10^{10}A·

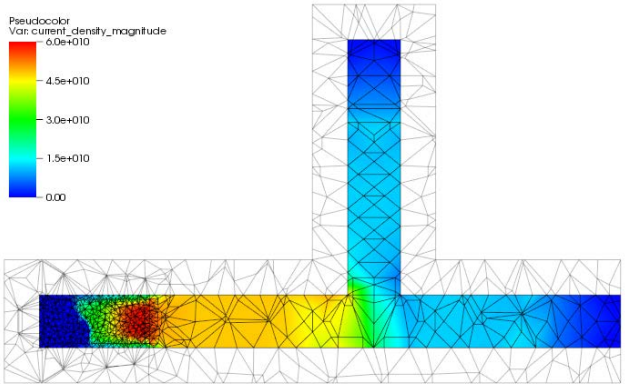

Figure 9: Current density vertical slice of the three-segment simulation.

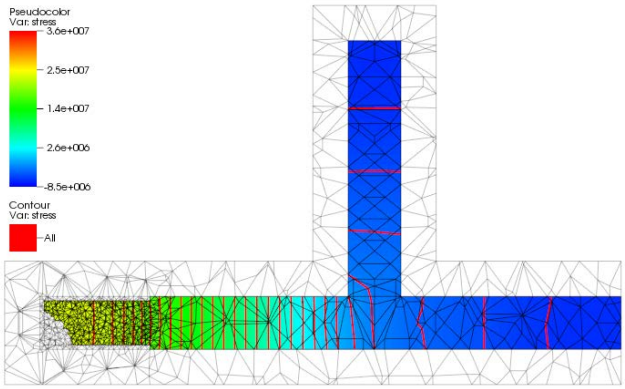

Figure 10: Hydrostatic vertical slice of the two-segment simulation.

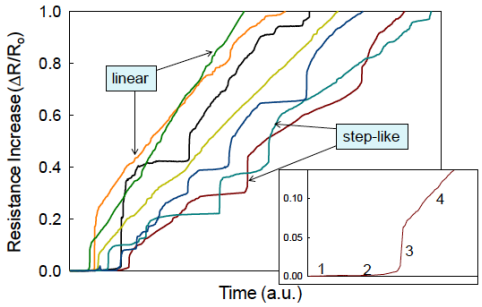

Figure 11: The normalized resistance change over time due to EM failure process. Courtesy of [27]

m^{-2} and $1 \times 10^{10} A \cdot m^{-2}$. As shown in Fig. 12, as void volume increases, a sharp resistance jump is observed at approximately 60 days of simulated time. Local operating temperature is also increased because of the Joule heating effect.

Figure 13 and 14 respectively show the current density and Joule heating power density distribution change as the void grows to cause failure. Notice that in the figures copper is surrounded by

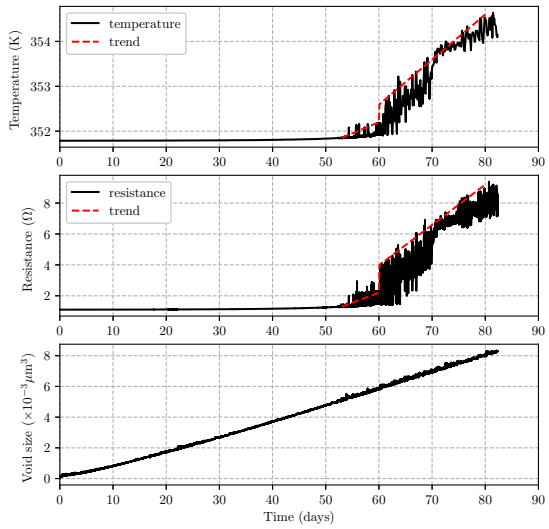

Figure 12: Temperature and resistance change over time (TO BE UPDATED)

liner material, which can be differentiated by recognizing the area where the current density is relatively low. At the moment the void cuts the copper interconnect, all current are forced to flow through liner material, which causes the rapid resistance increase. Fig. 14 also explains the reason of temperature increase. Initially, there is only one outstanding heat source located at the bottom of the via where the current has to flow through the thin liner between layers M1 and M2. After the void gains a significant volume, another heat source is created at the liner where the current is shunting through, as depicted by the temperature contour shown in Fig. 15. Therefore, with essentially another heat source introduced by void growing, a local temperature boost is also observed, which contribute to the resistance jump shown in Fig. 12.

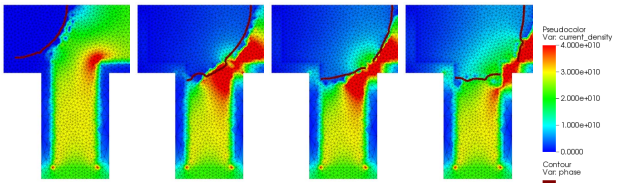

(a) $t = 18$ **(b)** $t = 60.1$ **(c)** $t = 60.15$ **(d)** $t = 65$

Figure 13: Current density as void growing. Time unit: day. Current density unit: $A \cdot m^{-2}$.

4.4 Void growth speed study

Fig. 12 also shows that the void volume grows at a roughly constant speed at $1.15 \times 10^{-9} \mu m^3 \cdot s^{-1}$. We compare this result with the void boundary velocity model proposed in work [13], where the boundary velocity (unit: $\mu m \cdot s^{-1}$) is calculated by

$$v_{\text{boundary}} = \frac{D_0 e^{-\frac{E_a}{k_B T}}}{k_B T} eZ\rho j. \tag{26}$$

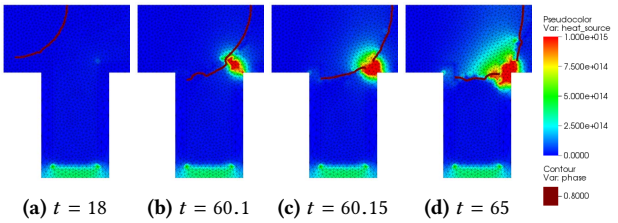

(a) $t = 18$ **(b)** $t = 60.1$ **(c)** $t = 60.15$ **(d)** $t = 65$

Figure 14: Power density (for Joule heating) change as void growing. Time unit: day. Power density unit: $\mathrm{W} \cdot \mathrm{m}^{-3}$.

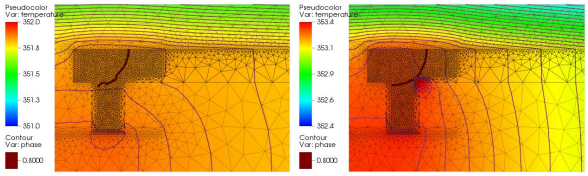

(a) $t = 60.1$ **(b)** $t = 60.15$

Figure 15: Temperature distribution and contour as void growing. Time unit: day. Temperature unit: K.

To compare between the results here, we need to provide the cross section area of copper interconnect, which is $0.2\mu\mathrm{m} \times 0.15\mu\mathrm{m} = 0.03\mu\mathrm{m}^2$, to reconcile the unit difference. In our 3D FEM simulation, the activity energy used is $E_a = 0.9\mathrm{eV}$. With this E_a applied to equation (26), it will result an equivalent void boundary speed of $1.72 \times 10^{-9}\mu\mathrm{m}^3 \cdot \mathrm{s}^{-1}$. This is significantly larger than the result $(1.15 \times 10^{-9}\mu\mathrm{m}^3 \cdot \mathrm{s}^{-1})$ obtained by the proposed simulator, which implies that the proposed method will deliver electromigration induced life time analysis that not as pessimistic as the existing modeling work [13].

5 CONCLUSION

A 3D finite element (FEM) multiphysics simulation method is proposed to investigate the electromigration effect and its failure characteristics in copper interconnects in modern integrated circuits. This work focuses on void growth simulation of the post-voiding stage of the electromigration induced failure process. Three physics systems — hydrostatic stress, current density, and temperature — are taken into account while the void growth is simulated. The software is designed to be easy to configure, scriptable, and highly compatible with the widely-used input and output formats. Experiments confirms that the proposed simulation method is capable to handle arbitrary interconnect shapes. Compared with real data observed in interconnect wear-out experiments, the new 3D FEM can correctly predict the resistance jump and Joule heating effect in the failure process. We also showed that the simulated void growth speed is less conservative than recently proposed compact EM model.

REFERENCES

[1] Martin S. Alnæs, Jan Blechta, Johan Hake, August Johansson, Benjamin Kehlet, Anders Logg, Chris Richardson, Johannes Ring, Marie E. Rognes, and Garth N. Wells. 2015. The FEniCS Project Version 1.5. *Archive of Numerical Software* 3, 100 (2015). https://doi.org/10.11588/ans.2015.100.20553

[2] Hussam Amrouch and Jörg Henkel. 2018. Estimating and Optimizing BTI Aging Effects: From Physics to CAD. In *Proc. Int. Conf. on Computer Aided Design (ICCAD).*

[3] T. Bergman, A. Lavine, F.P. Incropera, and D.P. DeWitt. 2011. *Fundamentals of Heat and Mass Transfer.* John Wiley & Son.

[4] Deepali N Bhate, Allen F Bower, and Ashish Kumar. 2002. A phase eld model for failure in interconnect lines due to coupled di usion mechanisms. *Journal of The Mechanics and Physics of Solids* (July 2002), 1–27.

[5] J. R. Black. 1969. Electromigration-A brief survey and some recent results. *IEEE Transactions on Electron Devices* 16, 4 (1969), 338–347.

[6] I. A. Blech. 1976. Electromigration in thin aluminum films on titanium nitride. *Journal of Applied Physics* 47, 4 (1976), 1203–1208.

[7] C. Chen, S. X.-D. Tan, J. Peng, T. Kim, and J. Chen. 2017. Analytical modeling of electromigration failure for VLSI interconnect tree considering temperature and segment length effects. *IEEE Transaction on Device and Materials Reliability (T-DMR)* 17, 4 (Dec. 2017), 653–666.

[8] H. Chen, S. X.-D. Tan, X. Huang, T. Kim, and V. Sukharev. 2016. Analytical Modeling and Characterization of Electromigration Effects for Multibranch Interconnect Trees. *IEEE Transactions on Computer-Aided Design of Integrated Circuits and Systems* 35, 11 (2016), 1811–1824.

[9] Y.K. Cheng, C.H. Tsai, C.C. Teng, and S.M. Kang. 2000. *Electrothermal Analysis of VLSI Systems.* Kluwer Academic Publishers.

[10] C. Cook, Z. Sun, E. Demircan, M. D. Shroff, and S. X.-D. Tan. 2018. Fast Electromigration Stress Evolution Analysis for Interconnect Trees Using Krylov Subspace Method. *IEEE Transactions on Very Large Scale Integration (VLSI) Systems* (2018).

[11] Christophe Geuzaine and Jean-François Remacle. 2009. Gmsh: A 3-D finite element mesh generator with built-in pre-and post-processing facilities. *International journal for numerical methods in engineering* 79, 11 (2009), 1309–1331.

[12] C-K Hu, MB Small, and PS Ho. 1993. Electromigration in Al (Cu) two-level structures: Effect of Cu and kinetics of damage formation. *Journal of applied physics* 74, 2 (1993), 969–978.

[13] X. Huang, A. Kteyan, X. Tan, and V. Sukharev. 2016. Physics-based Electromigration Models and Full-chip Assessment for Power Grid Networks. *IEEE Transactions on Computer-Aided Design of Integrated Circuits and Systems* 35, 11 (Feb. 2016), 1848–1861. https://doi.org/10.1109/TCAD.2016.2524540 DOI.

[14] ITRS 2014. International Technology Roadmap for Semiconductors (ITRS), 2014 Update. http://public.itrs.net.

[15] M A Korhonen, P Borgesen, D D Brown, and Che-Yu Li. 1993. Microstructure based statistical model of electromigration damage in confined line metallizations in the presence of thermally induced stresses. *Journal of Applied Physics* 74, 8 (1993), 4995–11.

[16] M. A. Korhonen, P. Bo/rgesen, K. N. Tu, and C.-Y. Li. 1993. Stress evolution due to electromigration in confined metal lines. *Journal of Applied Physics* 73, 8 (1993), 3790–3799.

[17] J. Lienig and M. Thiele. 2018. *Fundamentals of Electromigration-Aware Integrated Circuit Design.* Springer.

[18] A.K.M. Mahfuzul and Hidetoshi Onodera. 2018. PVT^2: Process, Voltage, Temperature and Time-dependent Variability in Scaled CMOS Process. In *IEEE/ACM International Conference on Computer-Aided Design (ICCAD).*

[19] Daniel Mueller-Gritschneder, Uzair Sharif, and Ulf Schlichtmann. 2018. Performance and Accuracy in Soft-Error Resilience Evaluation using the Multi-Level Processor Simulator ETISS-ML. In *Proc. Int. Conf. on Computer Aided Design (ICCAD).*

[20] Ennis T Ogawa, Ki-Don Lee, Volker A Blaschke, and Paul S Ho. 2002. Electromigration reliability issues in dual-damascene Cu interconnections. *IEEE Transactions on reliability* 51, 4 (2002), 403–419.

[21] Valeriy Sukharev, Armen Kteyan, and Xin Huang. 2016. Postvoiding stress evolution in confined metal lines. *IEEE Transactions on Device and Materials Reliability* 16, 1 (2016), 50–60.

[22] Valeriy Sukharev, Armen Kteyan, and Ehrenfried Zschech. 2012. Physics-Based Models for EM and SM Simulation in Three-Dimensional IC Structures. *IEEE Trans. on Device and Materials Reliability* 12, 2 (2012), 272–284.

[23] Z. Sun, E. Demircan, M. D. Shroff, C. Cook, and S. X.-D. Tan. 2018. Fast Electromigration Immortality Analysis for Multi-Segment Copper Interconnect Wires. *IEEE Transactions on Computer-Aided Design of Integrated Circuits and Systems* (2018).

[24] S. X.-D. Tan, H. Amrouch, T. Kim, Z. Sun, C. Cook, and J. Henkel. 2017. Recent advances in EM and BTI induced reliability modeling, analysis and optimization. *Integration, the VLSI Journal* (2017). https://doi.org/10.1016/j.vlsi.2017.08.009 in press.

[25] Ruopeng Wang, Thomas Benner, Alma Gregory Sorensen, and Van Jay Wedeen. 2007. Diffusion toolkit: a software package for diffusion imaging data processing and tractography. In *Proc Intl Soc Mag Reson Med*, Vol. 15. Berlin.

[26] X. Wang, H. Wang, J. He, S. X.-D. Tan, Y. Cai, and S. Yang. 2017. Physics-based Electromigration Modeling and Assessment for Multi-Segment Interconnects in Power Grid Networks. In *Proc. Design, Automation and Test In Europe. (DATE).*

[27] L. Zhang. 2010. *Effects of Scaling and Grain Structure on Electromigration Reliability of Cu Interconnects.* Ph.D. Dissertation. University of Texas at Austin.

[28] H. Zhao and S. Tan. 2018. Postvoiding FEM Analysis for Electromigration Failure Characterization. *IEEE Transactions on Very Large Scale Integration (VLSI) Systems* (2018).